

# On the Possible Detection of Low Frequency Periodic Signals in Gravitational Wave Interferometers

Adrian C. Melissinos

*Department of Physics and Astronomy, University of Rochester  
Rochester, NY 14627-0171, USA*

11/10/2014

## Abstract

We carried out a computer simulation of a large gravitational wave (GW) interferometer using the specifications of the LIGO instruments. We find that if in addition to the carrier, a single sideband offset from the carrier by the fsr frequency (the free spectral range of the arm cavities) is injected, it is equally sensitive to GW signals as is the carrier. The amplitude of the fsr sideband signal in the DC region is generally much less subject to noise than the carrier, and this makes possible the detection of periodic signals with frequencies well below the so-called “seismic wall”. The simulation also explains the observation of tidal gradients, with typical frequencies of  $10^{-5}$  Hz, and strain equivalent  $h \sim 10^{-22}$ , recorded during the LIGO S5 run and reported for the LSC in [1].

## 1 Introduction

It is often stated that the sensitivity of gravitational wave interferometers, as currently operated, is limited to frequencies above  $\sim 40$  Hz because of ground vibration and other noise in the DC region. Nevertheless, very low frequency gravity gradients acting on the interferometer have been extracted from the data. Such observations can be facilitated by examining the response of a sideband displaced from the carrier by one free spectral range,  $\nu_1 = \nu_0 + \nu_{fsr}$ , where  $\nu_{fsr} = c/2L$  with  $L$  the length of the interferometer arms. The observable signal is a phase difference due to the travel time in the two arms, induced by either: (1) the motion of the “free” end mirrors, caused by the passage of an appropriately polarized gravitational wave, or (2) the presence of differential gravity gradients in the two arms which modify the phase velocity of the propagating light, or (3) geophysical effects that physically displace the suspension of the end mirrors (test masses). In case (1) we speak of the “indirect” coupling of the GW to the interferometer, while in (2) the gravitational potential (associated with the gradient) couples “directly” to the light circulating in the arms. In GW interferometers, the induced time-dependent phase difference imposes audio sidebands on the light circulating in the arms. The circulating optical field can be either the carrier or the above mentioned  $\nu_1$  sideband. The  $\nu_1$  sideband has been chosen because it resonates in the arms and its transfer function is the same as that of the carrier. This is well known, and indicated in Fig.1 where the transfer function, from end-mirror motion to the demodulated amplitude at the dark port of the interferometer, is shown for both the carrier

and the  $\nu_1$  sideband, as a function of the excitation frequency.

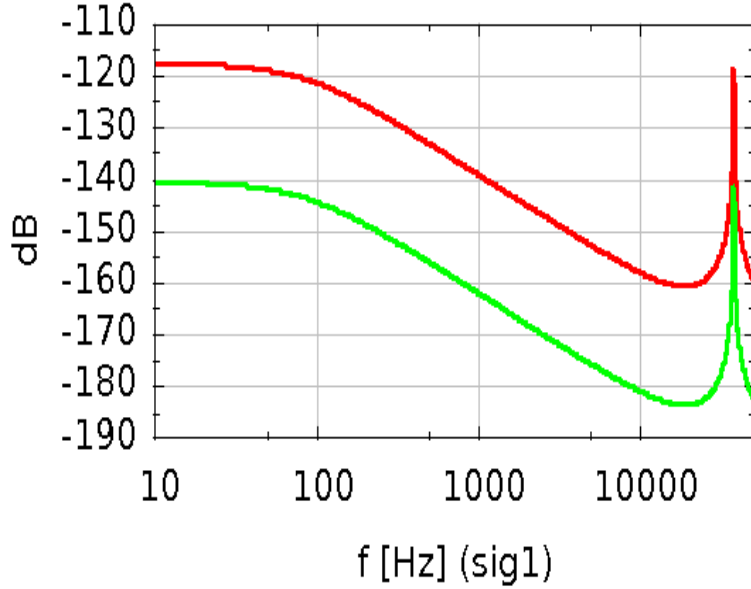


Figure 1: The transfer function, from end-mirror motion to the demodulated amplitude at the dark port of the interferometer, for both the carrier (red) and the  $\nu_1$  sideband (green), as a function of excitation frequency. The difference in scale is due to the different power entering the interferometer at the carrier and at the sideband frequencies.

The plots were generated with an excitation of strain  $h \sim 10^{-19}$  and as expected, the response is flat below  $f \sim 100$  Hz. The difference in scale results from the different power entering the interferometer at the two frequencies.

With the interferometer on a dark fringe, the audio sideband imposed on the carrier, is detected by mixing (in the photodetector) the carrier with the radio frequency (rf) sidebands, and then demodulating the photocurrent at the rf frequency. If the photodetector output is sampled fast enough, the spectrum of demodulated frequencies will extend beyond  $\nu_{fsr}$ . The light at the sideband frequency,  $\nu_1$ , contains the audio sidebands just as does the carrier, and the audio sidebands appear in the spectrum, symmetrically displaced about the  $\nu_{fsr}$  line. The audio sidebands can be extracted by demodulating the signal in the fsr region at the injected  $\nu_{fsr}$  frequency. Alternately, when the power in the demodulated signal in the  $\nu_{fsr}$  region is plotted as a time series it will be amplitude modulated at the audio frequency. Spectral analysis of the time series then reveals the frequency and amplitude of the audio sidebands. The advantage of extracting the audio signal from the  $\nu_{fsr}$  amplitude, rather than from the carrier, is that the low frequency disturbances that dominate the demodulated carrier signal at  $\nu \lesssim 40$  Hz, are suppressed in the fsr region. Of course noise arising from mirror motion will be present on both the carrier and on the fsr sideband. However, since the interest is in low frequency periodic signals, when spectrally analyzing the time

record of the  $\nu_{fsr}$  power to identify the audio sidebands, long integration times can be used, further reducing low frequency random noise. Signals at frequencies as low as  $\nu \sim 10^{-8}$  Hz, have been identified.

The demodulated amplitude in the region of the fsr frequency is the sum of the amplitude due to the fsr sideband  $A_{fsr}$  and the audio sideband amplitude  $A_\omega$  imposed on it. Thus the power in the fsr frequency region

$$P = |A_{fsr} + A_\omega|^2 = |A_{fsr}|^2 + 2|A_{fsr}||A_\omega|\cos(\omega t + \phi) + |A_\omega|^2,$$

modulated at the audio sideband frequency  $\omega$ . The modulation depth,  $M$ , is

$$M = \frac{P_{max} - P_{min}}{P_{max} + P_{min}} = 2 \frac{|A_{fsr}||A_\omega|}{|A_{fsr}|^2 + |A_\omega|^2}$$

is a measure of the audio amplitude since  $|A_{fsr}|$  is fixed and can be directly measured. For small values of  $|A_\omega|/|A_{fsr}|$ , such as prevailed during the S5 run,  $M \approx 2|A_\omega|/|A_{fsr}|$ . In this case, to detect weak audio amplitudes  $A_\omega$  it is desirable to keep  $A_{fsr}$  as small as possible.

To minimize  $A_{fsr}$  at the detection port, the paths that the fsr sideband  $A_{\nu_1}$  follows in returning from the two arms to the photodiode should lead to destructive interference. For the interferometer to be on a dark fringe for the **fsr sideband**, it is not sufficient for the carrier to be on a dark fringe, but it is also necessary that the macroscopic difference between the two paths be null. The macroscopic path difference is

$$\Delta z = \delta l + N\Delta L,$$

where  $\delta l$  is the imposed ‘‘Schnupp’’ asymmetry in the recycling cavity,  $\Delta L$  is the length difference between the arms, typically of order 2 cm for the LIGO interferometers during the S5 run, and  $N$  the effective number of round trips in the arms. If  $\Delta z$  is different from zero, the fsr sidebands arriving at the detection port will have a phase difference

$$\Delta\phi_1 = 2\pi \frac{\Delta z}{\lambda_1} = 2\pi \frac{\Delta z}{c} (\nu_0 \pm \nu_{fsr}) = \pm 2\pi \frac{\Delta z}{2L}$$

The last equality follows because, by definition, for the locked interferometer  $2\pi\Delta z/\lambda_0 = 0$ , modulo  $2\pi$ , and  $\nu_{fsr} = c/2L$  with  $L$  the length of the arms. Reducing  $\Delta\phi_1$  to null, is discussed in the following section.

Another concern is that if both the upper fsr sideband,  $\nu_{1+}$ , and the lower one,  $\nu_{1-}$ , are present, the audio sidebands imposed on the fsr sidebands cancel at the detection port. This can be seen in the ‘‘phasor’’ diagram of Fig.2; here the vectors representing the fsr sidebands are taken along the real axis and  $180^\circ$  out of phase, as is the case when generated by an electro-optic modulator. The two induced audio sidebands, the positive frequency (advanced) and the negative frequency (retarded), are shown superimposed on both fsr sidebands. Thus, the real part of the phasors always cancel, and so does the field at the audio frequency. To study the audio signal imposed on  $\nu_1$ , it is necessary to inject only **a single**

fsr sideband, for instance  $\nu_1 = \nu_0 + \nu_{fsr}$ .

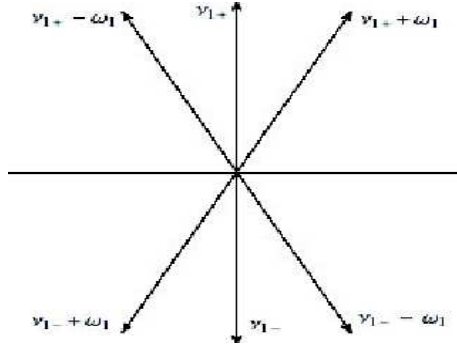


Figure 2: Phasor diagram for the upper  $\nu_{1+}$  and lower  $\nu_{1-}$  fsr sidebands when aligned along the real axis, and with the audio sidebands superimposed. When both fsr sidebands are present, the real part of the audio phasor vanishes.

The modulation of the signal at the fsr sideband frequency,  $\nu_{fsr}$  was observed by the LIGO collaboration and has been discussed in the past [1, 2]. Attempts to address the issue analytically can be found in [3, 4]. However, given the complexity of the optical fields in GW interferometers, it is advisable to carry out a numerical simulation such as presented here.

## 2 The numerical simulation

We have adopted the code FINESSE [5] which uses a standard matrix inversion algorithm to solve for the fields in the interferometer, as also done in TWIDDLE [6]. FINESSE includes a wide range of useful options and is easy to use. We simulated a “standard” recycled interferometer with 4 km long Fabry-Perot cavities in the arms, using the optical and other parameters of the H1 (Hanford) LIGO interferometer in the configuration of the S5 run [7]. The layout of the elements of the interferometer, and the labeling of the “nodes” used in the code are shown in Fig.3. We have included rf sidebands at  $\nu_{rf} = 24.480954$  MHz, with modulation index 0.4, and a **single** fsr sideband at  $\nu_{fsr} = 37.473$  kHz (as expected for an arm length of 4,000 m), with modulation index 0.3. A Schnupp asymmetry of 278 mm (the nominal value for S5) is included.

The results of the simulation are shown as graphs generated by the code, either as fixed values or as scans over some range of a particular parameter of an element in the interferometer. In most cases we examine the signals at the detector (AS) port, and plot the demodulated power at a specific frequency, after demodulating with one, two, or three frequencies. Occasionally, we give field amplitudes at a particular frequency, or the total power at different points (nodes) in the interferometer. Power is given in Watts, amplitudes in  $\sqrt{W}$ , and the carrier input from the laser was set to 1 W. The end mirrors (or any element) of the interferometer can be moved sinusoidally (shaken) at a specified frequency and with specified

amplitude; the driving amplitude is given in degrees of phase, namely  $\Delta x = \lambda/360 \approx 3 \times 10^{-9}$  m, which for the end mirrors is equivalent to strain  $h \approx 10^{-12}$ .

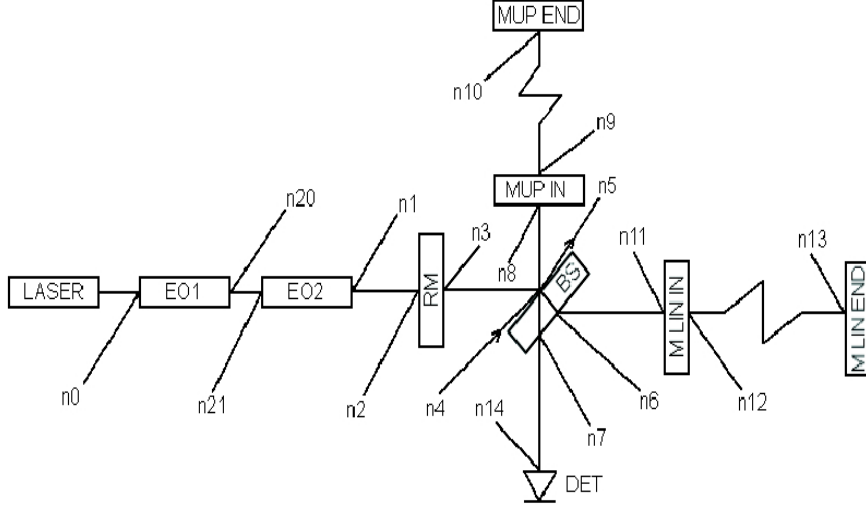


Figure 3: Layout of the elements of the interferometer, and the labeling of the “nodes” as used in the simulation code

In the simulation the two end mirrors were shaken differentially. One feature of FINESSE is that for the carrier the phase at any node is always zero (i.e. microscopically all distances are taken to be integers of the carrier wavelength), unless specified otherwise by the user through the addition of a phase at the particular node.

The interferometer is set on a dark fringe by choosing the phases of the cavity mirrors appropriately: for the in-line arm, input mirror  $\phi = 90^\circ$ , end mirror  $\phi = 270^\circ$ ; for the up-going arm, input mirror  $\phi = 0^\circ$  and end mirror  $\phi = 180^\circ$ . To place the fsr sideband ( $\nu 1$ ) on a dark fringe we adjust the length of the in-line arm to minimize the  $\nu 1$  amplitude at the detection port, which happens when  $L_{in-line} = 3999.998$  m, namely when the in-line cavity arm is shorter than the up-going arm by 2 mm. This is as expected because it compensates for the Schnupp asymmetry which is set with the in-line recycling cavity arm longer than the up-going arm by 278 mm. Taking the effective number of traversals in the arms as  $N \approx 140$ ,  $\Delta z = \delta l + N\Delta L \approx 0$ . This is indicated in Fig.4 where the demodulated fsr power (at the detection port) is shown as a function of the arm-length of the in-line cavity. We have limited the resolution of the scan to 1 mm, which can be maintained during interferometer operation without active feedback.

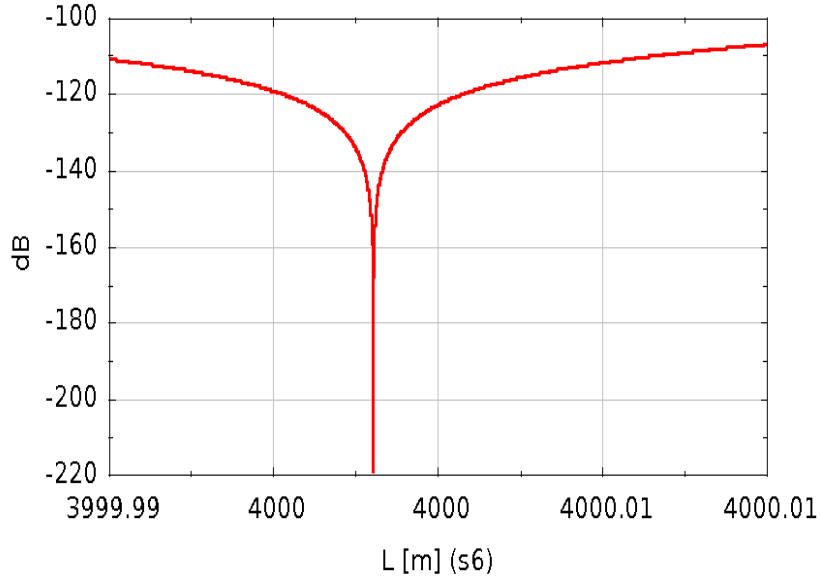


Figure 4: Demodulated power of the fsr sideband at the detection port as a function of the macroscopic length of the in-line arm

The field amplitudes and demodulated power at the detection port for this particular tuning  $\Delta L = L_{in} - L_{up} = -2$  mm, are given in Fig.5 . The red line is the demodulated carrier power, and at -360 db it is indeed dark. The demodulated power of the fsr sideband is shown by the blue line and at -160 db it is adequately dark, given the 1 mm resolution chosen for the setting of the macroscopic arm length difference. The green line shows the amplitude of the single fsr sideband. These fields are present in the absence of a driving signal, and with the interferometer in lock. We also checked that the simulation yields the correct power gains in the arm cavities,  $g_0^{arm} = 141$  for the carrier, and  $g_1^{arm} = 140$  for the fsr sideband; in the recycling cavity the carrier gain is  $g_0^{rc} = 111$ , and for the fsr sideband  $g_1^{rc} = 100$ .

To indicate how the fsr sideband is filtered by the arm cavities and the recycling cavity, we show in Fig.6 the fsr sideband demodulated power at the detection port as a function of the frequency offset from the carrier. The dominant width of the response is due to the spectral width of the arm cavities, the so called “cavity pole”. However at the exact fsr frequency, the effect of the recycling cavity becomes important giving rise to the inverted narrower structure, referred to as the “double cavity” pole.

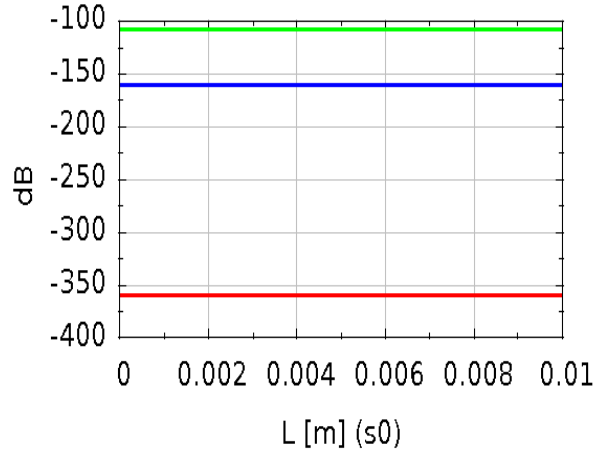


Figure 5: Field amplitude and demodulated power at the detection port for optimal tuning and in the absence of excitation. Demodulated carrier power (red), demodulated fsr sideband power (blue), amplitude of the single fsr sideband (green).

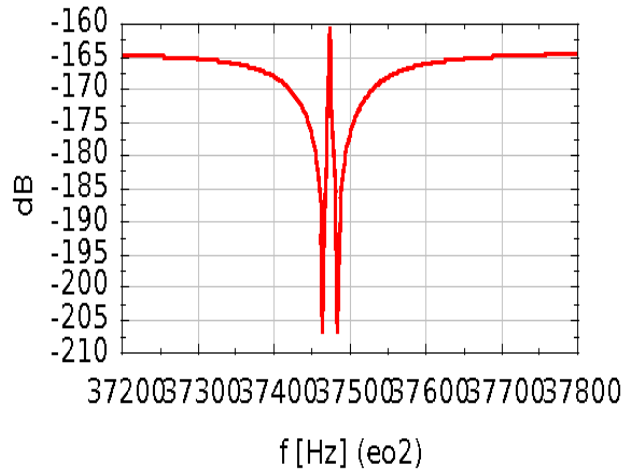


Figure 6: The fsr demodulated power at the detection port as a function of the frequency offset (from the carrier) of the injected sideband signal, and for “optimal tuning” of the arm length. See the text for details.

We now turn to the excitation of the interferometer by sinusoidally displacing the end mirror of both cavities in a differential manner, that is with opposite phases, as expected for a suitably polarized GW. We report the “triply” demodulated power at the detection port. By this we mean first demodulation at the rf frequency, followed by demodulation at the fsr frequency, since we are interested in the audio signal superimposed on the fsr sideband; thirdly we demodulate at the driving frequency, in order to obtain the response of the interferometer to the imposed “shaking” (excitation) of the end mirrors. In Fig.7 the red line

gives the response when demodulating the carrier (the usual signal), while the green line gives the response when demodulating at the fsr sideband frequency. The horizontal axis is in degrees of phase angle at the end mirrors. As already mentioned one degree corresponds to a strain  $h \approx 10^{-12}$ . Thus the horizontal scale spans  $h \sim 10^{-18}$  to  $10^{-16}$ . On this scale the response is linearly dependent on the excitation amplitude, and the fsr sideband carries the same information about the excitation as does the carrier. The frequency of the excitation used to generate the signal amplitudes shown in Fig.7 was 1 Hz, but as indicated in Fig.1 the response is flat below 10 Hz, for both the carrier and the fsr sideband. The difference in scale between the carrier and the fsr sideband is determined by the power injected at the two frequencies, as already mentioned in relation to Fig.1.

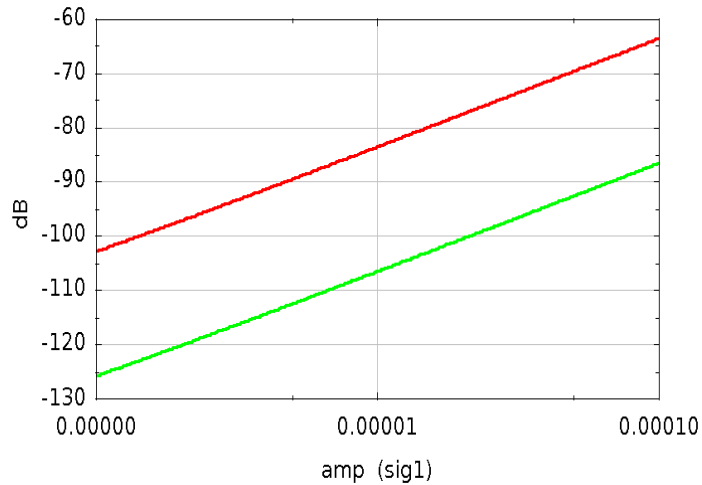


Figure 7: Carrier demodulated power (red) and fsr sideband demodulated power (green) as a function of the excitation of the arm end mirrors for the range of strain  $h \sim 10^{-18}$  to  $10^{-16}$ . The macroscopic arm length difference is set to the optimal value  $\Delta L = -2$  mm.

As a check of our understanding, when both fsr sidebands are allowed in the simulation, the demodulated fsr power, for the excitation used in Fig.7, is reduced by 200 db confirming the conclusion drawn from the graph in Fig.2.

### 3 Signal to Noise issues

To extract the audio signal from the  $\nu_1$  amplitude, we follow the approach described in the introduction, and that was also used in the analysis of the S5 run data: that is, we examine the modulation of the fsr power as a function of time. In the introduction we considered the case  $A_\omega \ll A_{fsr}$ . However when the fsr amplitude is minimized by adjusting the macroscopic arm length, the opposite may be true,  $A_\omega \gg A_{fsr}$ . The expression for the



modulation depth

$$M = \frac{P_{max} - P_{min}}{P_{max} + P_{min}} = 2 \frac{|A_{fsr}| |A_{\omega}|}{|A_{fsr}|^2 + |A_{\omega}|^2}$$

is valid in either case. When  $A_{\omega} \gg A_{fsr}$ , the signal at the audio frequency dominates and it is directly available. In Fig.8 we show the audio amplitude (green), the fsr amplitude (red) and the modulation depth,  $M$  (blue) for the same range of excitation amplitudes as used in Fig.7, namely in the range  $h \sim 10^{-18}$  to  $10^{-16}$  and at  $\nu_{audio} = 1$  Hz. In the simulation, the power at the fsr, is obtained by demodulating the photocurrent, at the detection port, at the rf frequency (24.480954 MHz), followed by demodulation at the fsr frequency (37.473 kHz). The power at the audio amplitude is obtained by following the same procedure as above, and then demodulating for a third time at the audio frequency used in the code to drive the end mirrors. The resulting  $A_{fsr}$  amplitude, is obviously independent of the external drive, while the power at  $A_{\omega}$  grows linearly with increasing excitation. When the two amplitudes are equal there is 100 percent modulation,  $M = 1$ .

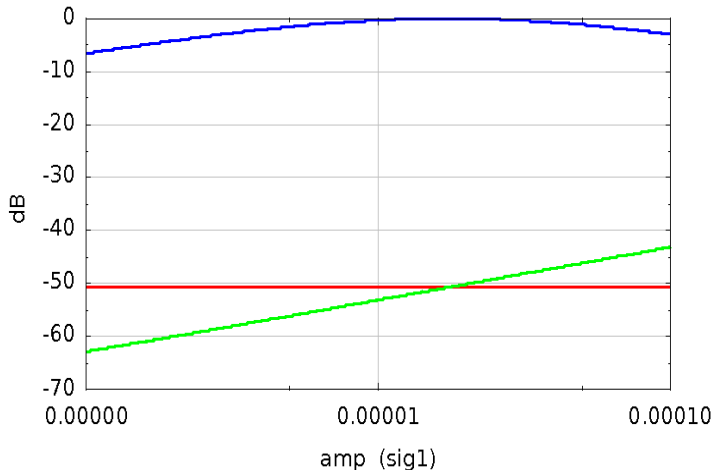


Figure 8: fsr sideband amplitude (red), audio amplitude (green), and modulation depth (blue), as a function of the excitation of the arm end mirrors for the range of strain  $h \sim 10^{-18}$  to  $10^{-16}$ . When the amplitudes are equal,  $M = 1$ . The macroscopic arm length difference is set to the optimal value  $\Delta L = -2$  mm.

The FINESSE code calculates the “noise over signal” ratio, N/S, (or its inverse) at any node in the interferometer by applying the Schottky formula to the total optical power at the node and comparing the associated noise power to the signal power at the particular frequency of interest. We have adopted the convention of presenting “noise over signal”, N/S, which is a spectral density and must be multiplied by  $\sqrt{BW}$  with BW the bandwidth used in the measurement, expressed in Hz. For the results presented here we use BW=1 Hz. Once the N/S is known for  $A_{\omega}$  and  $A_{fsr}$  the errors can be propagated to obtain the N/S for the modulation depth as well.

In these estimations we consider **only shot noise**, and this is justified because the photocurrent which is demodulated to yield the power at  $\nu = 37.473$  kHz is mainly free of the

disturbances near DC. Some of these disturbances are up-converted from the DC region to the fsr frequency region, but the up-converted amplitudes are typically few percent of  $A_{fsr}$  [8]. Up-converted discrete low frequency lines, such as due to the suspension of the optics, can be separated from the audio signal. Random (white) noise, is further suppressed when extracting the spectrum of periodic signals from a long time series of the power in the fsr frequency range: during the S5 LIGO run the time record was 16 months long.

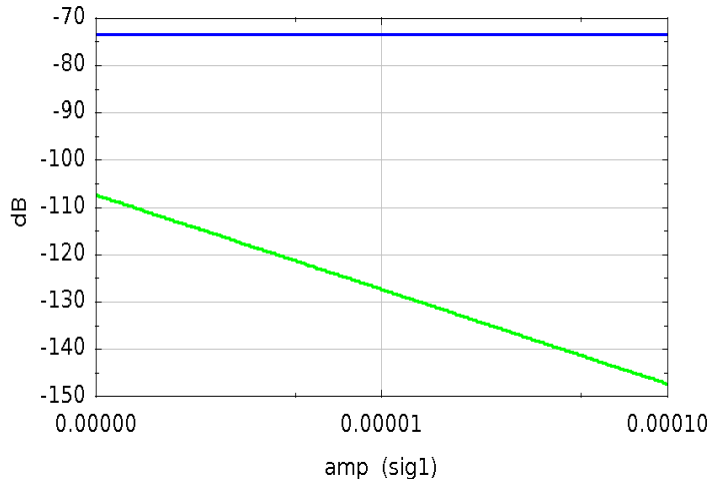


Figure 9: N/S for the audio demodulated power (green), N/S for the demodulated power at the fsr sideband (red), and N/S for the modulation depth (blue), as a function of the excitation of the arm end mirrors for the range of strain  $h \sim 10^{-18}$  to  $10^{-16}$ . The macroscopic arm length difference is set to the optimal value  $\Delta L = -2$  mm. As explained in the text, the red and blue lines overlap.

In Fig.9 we plot the N/S for the demodulated power at the audio frequency (green), the N/S for the power at the fsr sideband (red), and the N/S for the modulation depth (blue), for the same range of signal excitation as in Figs.7,8, namely for strain in the range  $h \sim 10^{-18}$  to  $10^{-16}$ . The red curve is not seen in Fig.9 because it is overwritten by the blue N/S line of the modulation depth. This is to be expected since for optimal tuning,  $A_{fsr} \ll A_{\omega}$ , and the N/S for  $A_{fsr}$  dominates the N/S for the modulation depth. For optimal tuning of the interferometer, and for strain  $h = 10^{-23}$  the signal to noise ratio, due only to shot noise, is  $S/N \approx 4$  for the signal extracted from the sideband, while it is  $S/N \approx 40$  for the signal extracted from the carrier.

## 4 Discussion

The response of the detected fsr power to an external excitation was observed serendipitously during the LIGO S5 run. In that run the fsr amplitude was recorded and demodulated as a separate channel in the detection chain, to search for a high frequency gravitational signal. Instead, the analysis of the fsr data revealed the slow modulation of the time series of the fsr

power at a frequency of  $\sim 10^{-5}$  Hz. In the S5 run there was no injection at the fsr sideband, but the sideband was spontaneously excited by parametric conversion from a nearby thermal (acoustic) resonance in the test masses (mirrors). The fsr sideband as well as the acoustic resonances can be seen in the first figure of [1]. The time series of the power in the fsr channel (integrated over the line width) for a 16-month long record is plotted in Fig.10; as seen in the inset it is modulated with a period of half a day and of one day. In retrospect, the presence of modulation indicates that only one, and not both sidebands are generated in the parametric conversion process<sup>1</sup>. Spectral (Fourier) analysis of the time record reveals 10 tidal lines, the observed frequencies being compared with their known values [9] in Table 1.

The spectra of the integrated power at the fsr are shown in Fig.11 for the region of diurnal frequencies and in Fig.12 for the semi-diurnal region.

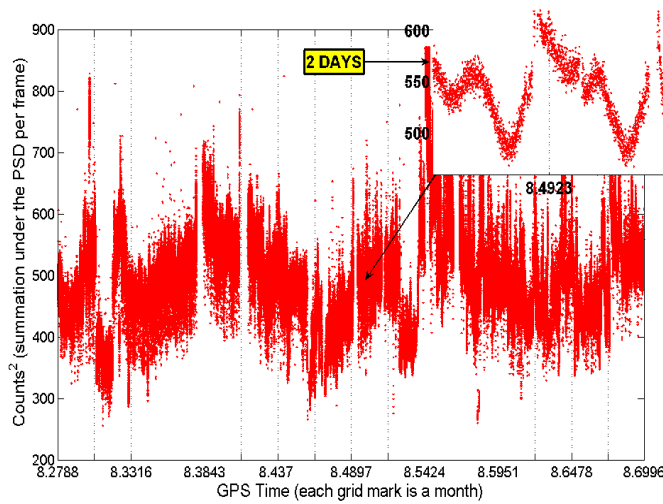


Figure 10: Integrated power in the free spectral range (fsr) region as a function of time, April 2006 to July 2007. The data are for the H1 interferometer and are sampled every 64 s. Note the daily and twice-daily modulation that can be seen in the inset. From [1].

<sup>1</sup>This can be attributed to the fact that the frequency of the acoustic resonance is slightly higher than the fsr frequency. Thus, preferentially only the upper sideband participates in the parametric conversion.

Table I. Observed and known frequencies of the tidal components (Hz)

Symbol	Measured	Predicted	L=lunar; S=solar
<u>Long period</u>			
S <sub>Sa</sub>	$6.536 \times 10^{-8}$	$6.338 \times 10^{-8}$	S declinational
<u>Diurnal</u>			
O <sub>1</sub>	$1.07601 \times 10^{-5}$	$1.07585 \times 10^{-5}$	L principal lunar wave
P <sub>1</sub>	$1.15384 \times 10^{-5}$	$1.15424 \times 10^{-5}$	S solar principal wave
S <sub>1</sub>	$1.15741 \times 10^{-5}$	$1.15741 \times 10^{-5}$	S elliptic wave of <sup>s</sup> K <sub>1</sub>
<sup>m</sup> K <sub>1</sub> , <sup>s</sup> K <sub>1</sub>	$1.16216 \times 10^{-5}$	$1.16058 \times 10^{-5}$	L,S declinational waves
<u>Twice-daily</u>			
N <sub>2</sub>	$2.19240 \times 10^{-5}$	$2.19442 \times 10^{-5}$	L major elliptic wave of M <sub>2</sub>
M <sub>2</sub>	$2.23639 \times 10^{-5}$	$2.23643 \times 10^{-5}$	L principal wave
S <sub>2</sub>	$2.31482 \times 10^{-5}$	$2.31481 \times 10^{-5}$	S principal wave
<sup>m</sup> K <sub>2</sub> , <sup>s</sup> K <sub>2</sub>	$2.31957 \times 10^{-5}$	$2.32115 \times 10^{-5}$	L,S declinational waves

As seen in the Table the measured tidal frequencies are in excellent agreement with their predicted value, within the resolution of the measurement. The uncertainty in the determination of the tidal frequencies is  $\Delta\nu_{res} = 1/(4T_{total}) = 6 \times 10^{-9}$  Hz, with  $T_{total} = 4.2 \times 10^7$  seconds; the factor of 4 being included because in the spectral analysis [10] the data was oversampled by a factor of four. Comparing the observed frequencies to the predicted ones, and using  $\Delta\nu_{res}$  as the measurement error, yields  $\chi^2/DF = 1.86$ . The table also includes a long-term, twice yearly, component which is evident by inspection of Fig.10.

The presence of the Earth tides is well known, and to keep the interferometer in lock, the end test masses must be mechanically displaced to correct for the tidal motion. Any residual uncompensated motion is corrected by the interferometer controls and can be observed in a long term analysis of the trends of the differential arm control signal (DARM-CTRL). However, the tidal acceleration has also a horizontal component along the arms, typically  $g_{hor} \approx 10^{-7}g \approx 10^{-6} \text{ m s}^{-2}$ , and this component is time-dependent at the tidal frequencies. This horizontal gravity gradient leads to a frequency shift of the light propagating along the arms, and thus to a cumulative phase shift for every traversal. In the weak field approximation, the presence of a gravitational potential  $\Phi$  modifies the  $g_{00}$  metric coefficient to

$$g_{00} = -(1 + 2\Phi/c^2) \quad (1)$$

The departure of  $g_{00}$  from its flat space value gives rise to time dilation, or equivalently to a shift in the frequency of light propagating through that gravitational field [11, 12].

$$\nu_A - \nu_B = -\frac{\Phi_A - \Phi_B}{c^2} \nu_A \quad \text{or} \quad \frac{\delta\nu}{\nu} = -\frac{\delta n}{n} = -\frac{\delta\Phi}{c^2}, \quad (2)$$

where we also introduced the refractive index of the light  $n = c'/c$ , which is often used in the literature.

A constant gradient  $g_{hor}$  along the  $x$ -direction can be described by a potential,  $\Phi = g_{hor}x$ . Thus light executing a single round trip in an arm of length  $L$  acquires a phase shift (as compared to light traveling in a field-free region) equal to

$$\delta\phi_t^{single} = 2 \int \delta\omega dt = 4\pi\nu_0 \int_0^L \frac{\delta\nu}{\nu} \frac{dx}{c} = \frac{4\pi}{\lambda_0} \int_0^L \frac{\Phi}{c^2} dx = \frac{2\pi}{\lambda_0} \frac{g_{hor}L^2}{c^2}. \quad (3)$$

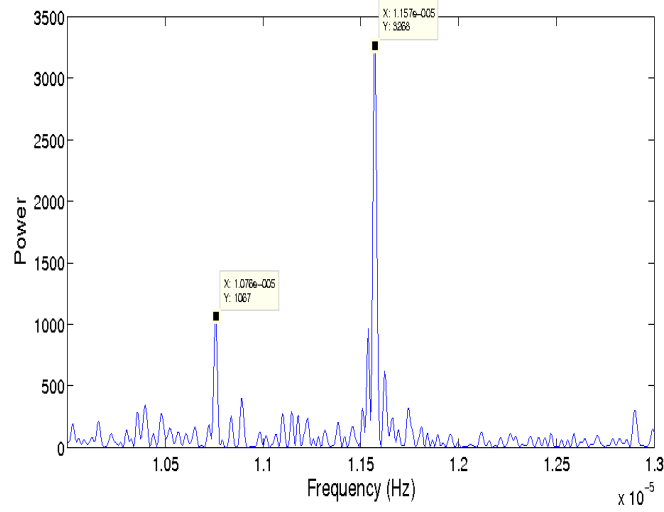


Figure 11: Frequency spectrum of the integrated fsr power in the diurnal region, from [1]. Note the fine structure.

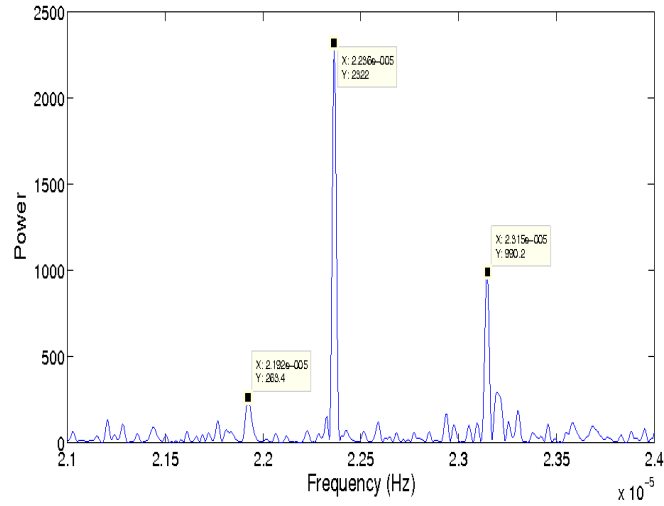


Figure 12: Frequency spectrum of the integrated fsr power in the twice daily region, from [1]. Note the fine structure.

Numerically, and without accounting for the multiple traversals, we find

$$\frac{\Delta\phi}{2\pi} \sim 2 \times 10^{-10}.$$

We can use this value to estimate the modulation depth expected for the LIGO S5 data. To this end we ran the simulation with a macroscopic arm length difference of  $\Delta L = 2$  cm (best estimate for the S5 run [8]), rather than the “optimal” value ( $\Delta L = -2$  mm) used in the simulations discussed so far. By introducing an excitation of  $7 \times 10^{-8}$  degrees, corresponding to the above value of  $\Delta\phi$ , we find a modulation depth of  $M = 0.18$ . This is in qualitative agreement with the data, and is additional evidence that the observed signals are due to the gravity gradient and not to uncompensated mirror motion. The advantage of using the modulation depth as a measure of the induced phase shift, is that it does not depend on the power input at the fsr sideband, since both the  $A_{fsr}$  and  $A_\omega$  amplitudes scale by the same factor.

In previous attempts to explain the modulation of the fsr power, macroscopic mirror motion was often considered [2, 3, 4]. Such motion, however, is compensated by the tidal servo and any remaining displacement is corrected by the interferometer controls. Instead, we now see that any external audio excitation, such as produced by the gravity gradients will simultaneously impose audio sidebands on both the carrier and on the fsr amplitude. The information carried by the fsr amplitude is the same as that carried by the carrier, except that the audio signals are now superimposed on a higher frequency signal which is displaced from the DC region where seismic noise and similar disturbances are dominant. The tidal signals have also been extracted from the minute trends of the signal controlling the differential arm separation (DARM-CTRL) but in that case the frequencies of the dominant lines are shifted by  $d\nu/\nu \approx 0.005$  and the weaker lines are absent. This may be due to the higher noise level when the low frequency signals are extracted from the carrier. Of course, the demodulation in the DC region performed on the carrier, is essential for sensing low frequency motion in order to keep the interferometer in lock. But once the interferometer is locked, when searching for low frequency audio signals, it is best to examine the demodulated power in the fsr amplitude.

## 5 G.W. signals from close binaries

As seen in Figs.11,12 the LIGO interferometers can detect weak signals at low frequencies  $\nu \sim 10^{-5}$  Hz, with excellent signal to noise ratio (SNR) . While the horizontal tidal gradient is large,  $\sim 10^{-6} \text{ ms}^{-2}$ , it is coupled to the interferometer through the “direct” effect imposing only a very small phase shift. An incoming GW (at a sufficiently high frequency) that would produce the same phase shift by acting on the “free” mirrors, would have a strain  $h = (\Delta\phi/2\pi)(\lambda/NL) \sim 5 \times 10^{-22}$ . Therefore it may be possible to detect the gravitational signal from close binaries that have typical periods of a fraction of a day or less.

The main difficulty is that at frequencies below the natural frequency of the suspension the test masses can not any more be treated as free. But not all is lost: the test masses

respond to the tidal acceleration imposed by the gravitational wave [13, 14]

$$\ddot{x} = \frac{1}{2}\ddot{h}(t)x$$

which is counteracted by the restoring acceleration of the pendular suspension. Letting  $\Omega, h$  be the angular frequency and amplitude of the gravitational wave, and  $\omega_s$  the pendular angular frequency, a direct calculation for the change in the arm length gives<sup>2</sup>

$$\Delta L(t) = -\frac{h_0 L}{2} \frac{1}{(\omega_s/\Omega)^2 - 1} e^{i\Omega t} \quad (4)$$

as compared to  $\Delta L(t) = (h_0 L/2)e^{i\Omega t}$  when  $\Omega \gg \omega_s$ , namely when the mirrors are free. We see that in calculating the phase shift in the interferometer, the strain of a low frequency gravitational wave must be derated<sup>3</sup> by  $(\Omega/\omega_s)^2$ .

For the majority of binaries,  $\Omega/2\pi \sim 10^{-5}$  Hz, while for LIGO  $\omega_s = 0.75$  Hz and for VIRGO  $\omega_s = 0.5$  Hz. Given the expected gravitational wave strain produced by binaries, a large improvement in interferometer sensitivity appears necessary to detect such sources. However, Brown et al. reported recently on a pair of detached white dwarfs with a period of  $T = 12.75$  minutes ( $\Omega/2\pi = 2.6 \times 10^{-3}$  Hz) [15]. The binary is located at a distance of 1 kpc, and the calculated gravitational wave strain at the Earth is  $h = 10^{-22}$ . To detect the source in one year of observation, the required sensitivity of the interferometer is

$$h/\sqrt{\text{Hz}} = 10^{-22}(\Omega/\omega_s)^2(6 \times 10^{-9})^{-1/2} \sim 4 \times 10^{-23}\sqrt{\text{Hz}}$$

for  $\omega_s = 0.5$  Hz. This seems achievable, and there may exist other binaries with even shorter periods, that have not as yet been detected optically but could be searched for, through their gravitational signal.

## 6 Acknowledgements

I wish to thank Daniel Sigg who designed and implemented the fsr read-out channel, and Fred Raab for his support and hospitality at the Hanford LIGO laboratory. Bill Butler, Chad Forrest, Tobin Fricke and Stefanos Giampanis were instrumental in the analysis. The excellent quality of the data is due to the dedicated efforts of the staff and operators at LHO, and of the members of the LSC collaboration. I also thank Valentin Rudenko of Moscow State University, for his encouragement and continuing interest in this work. I am indebted to the team that wrote and maintains the FINESSE code, and I thank Mark Bocko and Malik Rakhmanov for insightful comments on an earlier version of this paper.

---

<sup>2</sup>The following equation has the inverse behavior from that of the driven oscillator because the driving acceleration is proportional to  $\Omega^2$ .

<sup>3</sup>The direct coupling is always present, but the induced phase shift  $\Delta\phi = (khLN)(\Omega T)^2/6$ , scales as the square of the g.w. frequency.

## References

- [1] A. Melissinos (for the LSC), “The effect of the Tides on the LIGO Interferometers”, Twelfth Marcel Grossman Meeting on General Relativity, World Scientific, p.1718 (2012); arXiv:1001.0558.
- [2] Chad J. Forrest “Tidal effects on laser gravitational wave detectors”, Thesis, University of Rochester, and LIGO Document P0900003-v1 (2009).
- [3] A. V. Gusev and V. N. Rudenko, “Gravitational Modulation of the Optical Response of Long Baseline Laser Interferometers”, English translation, JETP Letters, **91**, 495 (2010).
- [4] A. V. Gusev, V. N. Rudenko and I. S. Yudin “Low frequency signals of large scale GW-interferometers”, arXiv:1310.3104, 11 Oct 2013, and in Russian, JETP **146**, 779 (2014).
- [5] Andreas Freise, “FINESSE”, [www.gwoptics.org/finesse](http://www.gwoptics.org/finesse).
- [6] M. W. Regehr, J.E. Mason and H. Yamamoto “Twiddle” Tech. report, Caltech, 1999; LIGO T990022.
- [7] J. Abadie et al. “Calibration of the LIGO Gravitational Wave Detectors in the Fifth Science Run”, Nucl.Instrum.Meth. **A624**: 223-240, 2010; C. Forrest, T. Fricke, S. Giampanis and A. Melissinos “Determination of the Frequency of the Earth Tides Using a LIGO Interferometer”, LIGO Document T080002-00-Z (2008).
- [8] William E. Butler “Characterization of the high frequency response of laser interferometer gravitational wave detectors”, Thesis, University of Rochester (2004).
- [9] P. Melchior “The Tides of the Planet Earth” Pergamon Press, 1978.
- [10] J. D. Scargle, ApJ **263**, 835 (1982); W. Press, W. Vetterling, S. Teukolsky and B. Flannery, “Numerical Recipes in C++”, Cambridge University Press, 1988.
- [11] S. Weinberg “Gravitation and Cosmology” John Wiley and Sons, NY, 1972.
- [12] J. B. Hartle “Gravity: an introduction to Einstein’s general relativity” Addison Wesley, San Francisco, 2003.
- [13] C.W. Misner, K.S. Thorne and J.A. Wheeler, “Gravitation” W.H. Freeman, San Francisco, 1970, Chapter 37.
- [14] M. Rakhmanov, Physical Review **D71**, 084003 (2005).
- [15] W.R. Brown et al. “A 12 minute orbital period detached white dwarf eclipsing Binary” ApJ Letters, **737**:L23 (2011), arXiv:1107.2389 (2011).